

# Observation of topological phase with critical localization in a quasi-periodic lattice

Teng Xiao,<sup>1,\*</sup> Dizhou Xie,<sup>1,\*</sup> Zhaoli Dong,<sup>1</sup> Tao Chen,<sup>1</sup> Wei Yi,<sup>2,3,†</sup> and Bo Yan<sup>1,4,5,‡</sup>

<sup>1</sup>*Interdisciplinary Center of Quantum Information,  
State Key Laboratory of Modern Optical Instrumentation,  
Zhejiang Province Key Laboratory of Quantum Technology and Device,  
Department of Physics, Zhejiang University, Hangzhou 310027, China*

<sup>2</sup>*CAS Key Laboratory of Quantum Information, University of Science and Technology of China, Hefei 230026, China*

<sup>3</sup>*CAS Center For Excellence in Quantum Information and Quantum Physics, Hefei 230026, China*

<sup>4</sup>*Collaborative Innovation Centre of Advanced Microstructures, Nanjing University, Nanjing, China, 210093*

<sup>5</sup>*Key Laboratory of Quantum Optics, Chinese Academy of Sciences, Shanghai, China, 200800*

(Dated: October 25, 2021)

Disorder and localization have dramatic influence on the topological properties of a quantum system. While strong disorder can close the band gap thus depriving topological materials of topological features, disorder may also induce topology from trivial band structures, wherein topological invariants are shared by completely localized states in real space. Here we experimentally investigate a fundamentally distinct scenario where a topological phase is identified in a critically localized regime, with eigenstates neither fully extended nor completely localized. Adopting the technique of momentum-lattice engineering for ultracold atoms, we implement a one-dimensional, generalized Aubry-André model with off-diagonal quasi-periodic disorder in momentum space, and characterize its localization and topological properties through dynamic observables. We then demonstrate the impact of interactions on the critically localized topological state, as a first experimental endeavour toward the clarification of many-body critical phase, the critical analogue of the many-body localized state.

Topologically protected edge modes in topological materials give rise to robust quantum charge transport against weak disorder [1, 2]. However, for sufficiently strong disorder, the band gap closes and all the eigenstates become localized under Anderson localization, rendering the system topologically trivial with vanishing transport [3–6]. Contrary to this well-accepted scenario, recent studies have shown that disorder can also induce topology in a trivial insulator, leading to a topological Anderson insulator where the global topology is carried by completely localized ground-state wave functions [7, 8]. Such intimate connections among topology, disorder, and localization stimulate intense research efforts in recent years [9–15], which culminate in the experimental observation of disorder-induced topological Anderson insulators in cold atoms [16] and photonics [17, 18].

Here we experimentally demonstrate an alternative scenario, where a topological phase exists in the critically localized regime. Different from either the extended state (as in Bloch waves) or the fully localized state (as in Anderson localization), a critically localized state features multifractal behaviors and unique eigenenergy spectral statistics [19–28], which, in the presence of many-body interactions, would give rise to a many-body critical region that interpolates the extended, ergodic phase and the fully localized, nonergodic many-body localized phase [29–32]. Signatures of the critically localized states have been theoretically identified in several models with stochastic or quasi-periodic disorder [22–28], which suggest an intriguing many-body state that is nonergodic but exhibits features pertaining to an

extended state [27, 28]. An experimental demonstration of such a phase, particularly in a many-body regime, is desirable but has remained elusive.

Taking advantage of the flexible control available to ultracold atomic momentum-lattice engineering [33–37], we implement a generalized Aubry-André model in one dimension, with quasi-periodic modulation in the nearest-neighbor hopping rate. While such an off-diagonal Aubry-André model with incommensurate hopping has been theoretically predicted to host both critically localized and extended phases [22, 27], we adopt a configuration where the quasi-periodic disorder also drives a topological phase transition [25, 26]. This allows us to study in detail the interplay between localization, topology, and interaction. Probing localization and topology through dynamic observables such as the dynamic inverse participation ratio (dIPR) and the mean chiral displacement (MCD) [16, 38], we identify a critically localized topological phase, bounded by extended topological phases and a critically localized trivial phase. We further explore the impact of inter-atomic interactions on the stability of the critical topological phase, paving the way toward a systematic study of the many-body critical state.

*Topology with critical localization:*— We consider a generalized Aubry-André model given by the tight-binding Hamiltonian

$$\hat{H}_0 = \sum_j [t + \lambda \cos(j+1)\pi + \delta \cos(2\pi\beta j + \varphi)] (\hat{c}_j^\dagger \hat{c}_{j+1} + \text{H.c.}), \quad (1)$$

where  $\hat{c}_j^\dagger$  ( $\hat{c}_j$ ) is the creation (annihilation) operator at site  $j$ . As illustrated in Fig. 1(a), the model resembles

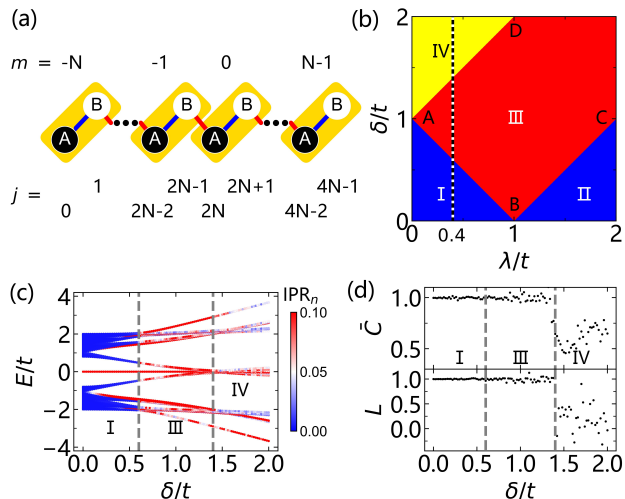


FIG. 1. Critically localized topological phase. (a) Schematic illustration of the off-diagonal Aubry-André model of Eq. (1). The lattice sites  $j$  are divided into unit cells (labeled by  $m$ ) with sublattice sites  $A$  and  $B$ , according to commensurate hopping terms in Eq. (1). (b) Theoretical phase diagram: regions I and II are the extended topological phase; region III is the critically localized topological phase; region IV is critically localized but topologically trivial. Different regions are separated by linear boundaries: AB ( $\delta/t = 1 - \lambda/t$ ), BC ( $\delta/t = \lambda/t - 1$ ), and AD ( $\delta/t = 1 + \lambda/t$ ). (c) Eigenenergy spectrum with increasing quasi-periodic disorder strength  $\delta/t$ , along the vertical dotted line in (b) with  $\lambda/t = 0.4$ . Color code indicates the value of  $\text{IPR}_n$ , defined in the main text. (d) Local topological marker (LTM) and time-averaged mean chiral displacement (A-MCD) along the vertical dotted line in (b). For numerical calculations in (c)(d), we take a lattice with 400 sites ( $N = 100$ , or 200 unit cells) under an open boundary condition. Without loss of generality, we set  $\varphi = 0$  in (c), while taking the average over 50 randomly generated  $\varphi$  in the range of  $[0, 2\pi)$  in (d). The A-MCD is calculated by further taking the time average over a time evolution initialized in the state  $|m = 0, A\rangle$  and with a duration of  $80\hbar/t$ .

a Su-Schrieffer-Heeger (SSH) model [39] with intra- and inter-cell hopping rates  $t - \lambda$  and  $t + \lambda$ , respectively, which are further dressed by an incommensurate hopping term with amplitude  $\delta$  and phase  $\varphi$ . We take  $\beta = (\sqrt{5} - 1)/2$  throughout the work, under which the incommensurate hopping constitutes the off-diagonal, quasi-periodic disorder.

In the absence of disorder ( $\delta = 0$ ), Hamiltonian (1) is reduced to the standard SSH model, where a topological phase transition occurs when  $\lambda$  crosses zero. In this work, however, we focus on the parameter region with  $\lambda > 0$  and consider the case where the system is topologically non-trivial for  $\delta = 0$ . In Fig. 1(b), we show the theoretical phase diagram [25, 26] (see also the Supplemental Information), where a critically localized topological phase (region III) is surrounded by extended topological phases (regions I and II) and a critically localized trivial phase (region IV).

For the  $n$ th eigenstate  $|\Psi_n\rangle = \sum_j \psi_n(j)c_j^\dagger|\text{vac}\rangle$  ( $|\text{vac}\rangle$  being the vacuum state and  $\psi_n(j)$  the wave function), its localization property is captured by the inverse participation ratio, defined as  $\text{IPR}_n = \sum_j |\psi_n(j)|^4$ . Physically,  $\text{IPR}_n$  is the inverse of the number of sites occupied by the  $n$ th eigenstate, with  $\text{IPR}_n = 0$  for an extended state and  $\text{IPR}_n = 1$  for a completely localized state. As shown in Fig. 1(c), across the localization transition boundary [AB in Fig. 1(b)],  $\text{IPR}_n$  typically changes from zero in region I to finite values in regions III and IV. Since  $\text{IPR}_n$  is finite but much smaller than unity in regions III and IV, the system therein is critically localized with fractal dimensions [25–28], rather than fully localized. A recent theoretical study on a related, generalized Aubry-André-Harper model suggests that, in a many-body setting, such a critically localized state turns into a many-body critical phase, which is nonergodic but exhibits distinct dynamics and entanglement-entropy scaling from those of a many-body localized state [27]. Note that, apart from a handful of edge states (see Supplemental Information), our model does not possess mobility edges.

To characterize topological properties, we adopt the local topological marker (LTM) [11, 16], defined through

$$L = \frac{1}{2} \text{Tr}'(\hat{Q}\hat{\Gamma}\hat{m}\hat{Q}), \quad (2)$$

where  $\text{Tr}'$  is the trace over a single unit cell deep in the bulk,  $\hat{m}$  is the unit-cell position operator,  $\hat{Q} = \hat{P}_+ - \hat{P}_-$ ,  $\hat{\Gamma} = \hat{\Gamma}_A - \hat{\Gamma}_B$ , where  $\hat{P}_+$  ( $\hat{P}_-$ ) is the projection operator onto the band with positive (negative) eigenenergies, and  $\hat{\Gamma}_A$  ( $\hat{\Gamma}_B$ ) projects onto the sublattice site  $A$  ( $B$ ) [see Fig. 1(a)]. The LTM can be dynamically probed through the MCD [16, 38, 40], defined as

$$C = 2\langle \hat{\Gamma}\hat{m} \rangle, \quad (3)$$

which is the expectation value of the chiral displacement operator  $\hat{\Gamma}\hat{m}$  with respect to the time-evolved state. Experimentally, we use the time-averaged mean chiral displacement (A-MCD)  $\bar{C}$  to characterize different topological phases, which converges faster in dynamics [37]. As shown in Fig. 1(c)(d), the numerically evaluated LTM and A-MCD are both close to the quantized value of 1 in regions I and III, revealing the topological nature of these regions. A topological phase transition occurs on the boundary of regions III and IV, as LTM and A-MCD are no longer quantized in region IV, indicating a topologically trivial regime. Note that neither LTM nor A-MCD vanishes in region IV, due to the apparent divergence of the localization length therein (see Supplemental Information). Remarkably, the critically localized topological phase (region III) occupies a large parameter regime on the phase diagram.

*Experimental implementation.*— We experimentally implement Hamiltonian (1) by engineering a one-dimensional momentum lattice of 16 sites ( $N = 4$ )

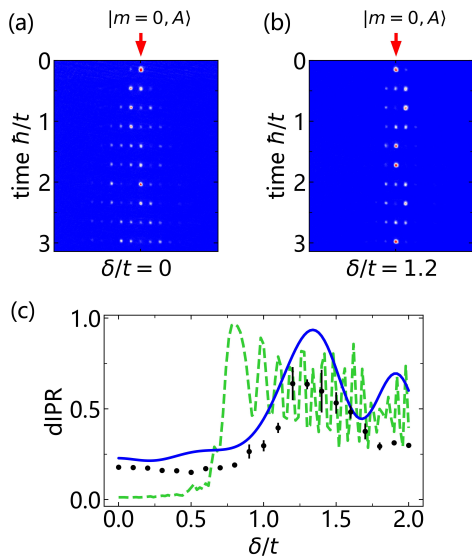


FIG. 2. Extended to critical transition. (a) Measured time evolution of atom-number distribution in momentum space in the extended phase with  $\delta/t = 0$ . (b) Time evolution of atom-number distribution in the critically localized state with  $\delta/t = 1.2$ . (c) Extended to critical transition probed through dIPR. Black dots are experimental data for an evolution time of 0.5ms along a momentum lattice with 16 sites. Blue line represents numerical results under the same parameters. Green-dashed line is the numerical results with 400 lattice sites, and with a longer evolution time of  $80\hbar/t$  ( $\sim 12.7$ ms under experimental parameters). We fix  $\lambda/t = 0.4$  and  $t/\hbar = 2\pi \times 1.0(1)$ kHz for all panels. Error bars show SE of mean.

in a  $^{87}\text{Rb}$  Bose-Einstein condensate (BEC) of about  $10^5$  atoms in a dipole trap with trapping frequencies  $2\pi \times (50, 160, 170)$ Hz [36, 41]. Discrete momentum states are coupled by a series of frequency-modulated, 1064nm Bragg-laser pairs along the weakly-trapped direction. The hopping amplitudes and phases between adjacent momentum-lattice sites are individually tuned by adjusting the Bragg-coupling parameters, which enables us to implement the quasi-periodic disorder straightforwardly. While for most of our experiments, we adopt a hopping amplitude  $t/\hbar \approx 2\pi \times 1$ kHz, we fix  $\varphi = 0$  for all experiments. Without further tuning, the inter-atomic interaction energy  $U/\hbar \approx 2\pi \times 0.7$ kHz, whose impact is small as  $U < t$  (see Supplemental Information). Here  $U = g\rho$ , where  $g = 4\pi\hbar^2 a/m$ ,  $\rho$  is the average density of the initial BEC evaluated with the Thomas-Fermi radius,  $a = 103a_0$  is the  $s$ -wave scattering length ( $a_0$  being the Bohr radius), and  $m$  is the atomic mass. However, as demonstrated later, interaction effects can be experimentally probed by tuning the ratio  $U/t$ .

For the time evolution, atoms of the condensate are initialized in the zero-momentum state, which corresponds to the lattice site  $|m = 0, A\rangle$ . We then switch on the Bragg lasers and let the condensate evolve in the mo-

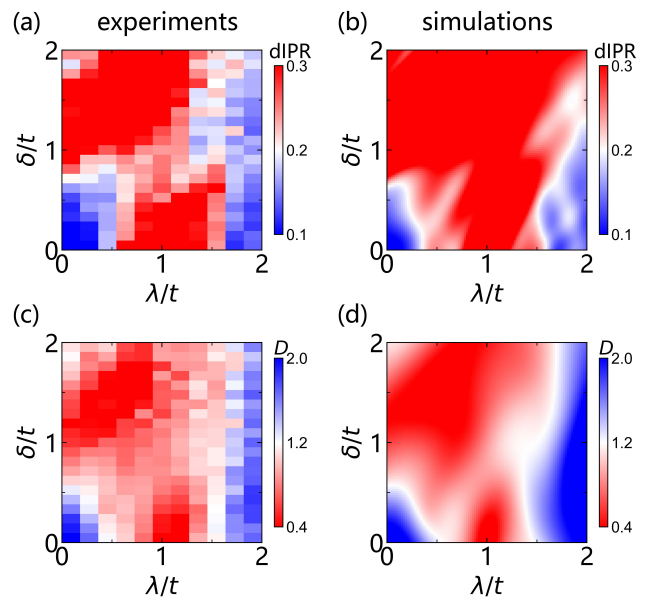


FIG. 3. Localization phase diagram. (a) Color contour of measured dIPR on the  $\delta$ - $\lambda$  plane. (b) Numerically calculated dIPR under the same parameters as (a). (c) Color contour of measured mean displacement  $D$ . (d) Numerically calculated  $D$ . Here we fix  $t/\hbar = 2\pi \times 1.0(1)$ kHz along a lattice with 16 sites, and with an evolution time of 0.5ms.

mentum lattice. At the end of the time evolution, we turn off the dipole trap and Bragg lasers, and take an absorption image of the atoms after 20ms time of flight in free space. This allows us to probe the atomic density distribution along the momentum lattice right before the time-of-flight, from which all dynamic quantities are extracted.

*Localization properties:*— Localization of eigen wave functions can be qualitatively probed through the dynamic propagation of the condensate. In the absence of disorder ( $\delta = 0$ ), all eigen wave functions are extended, apart from edge states which have negligible overlap with the initial state. This leads to the ballistic expansion observed in Fig. 2(a). By contrast, for sufficiently large  $\delta$ , all the eigen wave functions are critically localized, giving rise to the observed condensate localization near the initial site  $|m = 0, A\rangle$  [see Fig. 2(b)].

More quantitatively, we construct the dIPR from the time-evolved state  $|\Psi(t)\rangle = \sum_j \psi(j, t)c_j^\dagger|\text{vac}\rangle$  as

$$\text{dIPR} = \sum_j |\psi(j, t)|^4, \quad (4)$$

where  $\psi(j, t)$  is the time-evolved wave function on site  $j$ . A vanishing (finite) dIPR at long times indicates the extended (critical or local) nature of eigenstates that have support on the initially occupied lattice site  $|m = 0, A\rangle$ . Due the absence of mobility edge in our model, dIPR should therefore reflect the localization property of the

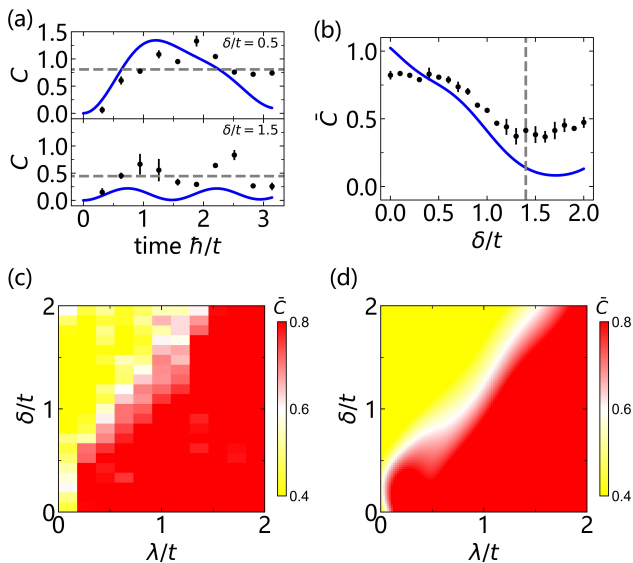


FIG. 4. Probing topological properties. (a) Time evolution of MCD in region I (upper panel with  $\delta/t = 0.5$ ), and region IV (lower panel with  $\delta/t = 1.5$ ). Black dots are experimental data, and blue lines represent numerical results under the same parameters. The gray lines are the averages of experimental data. (b) A-MCD  $\bar{C}$  as a function of  $\delta/t$ . Black dots are experimental data, and the blue line is from numerical simulation. The gray vertical line indicates the theoretical phase transition point  $\delta/t = 1.4$ . We fix  $\lambda/t = 0.4$  in (a)(b). Error bars show SE of mean. (c) Color contour of experimentally measured A-MCD. (d) Numerically calculated A-MCD. Other parameters are the same as those in Fig. 3.

eigenenergy spectrum. This is confirmed by numerical simulations for a sufficiently long evolution time [green-dashed curve in Fig. 2(c)], where an extended to critical transition can be identified near the theoretically predicted transition point  $\delta/t = 0.6$ . For a shorter, experimentally accessible evolution time, the transition is still visible in both the numerical and experimental results [blue curve and black dots in Fig. 2(c), respectively], albeit slightly shifted toward a larger disorder strength. Finally, for sufficiently large disorder, the observed dIPR appears to oscillate around a finite value well below unity, indicating the critically localized nature of the state.

We then map out the phase diagram for the critically localized state using our measured dIPR, as shown in Fig. 3(a). The phase diagram constructed from the dIPR measurements [ Fig. 3(a)] agrees well with our numerical simulation under the same parameters [ Fig. 3(b)], both consistent with the theoretical prediction in Fig. 1(b): the critically localized region occupies the majority of the phase diagram, with two extended regions located at the lower left and right corners, respectively. The phase diagram is further confirmed using the mean displace-

ment

$$D = \left[ \sum_{m,\sigma=A,B} m^2 n_{m,\sigma} \right]^{1/2}, \quad (5)$$

where  $n_{m,\sigma}$  is the fraction of atom population on sublattice site  $\sigma$  of unit cell  $m$ . We show our experimental data and numerical results in Figs. 3(c) and (d), respectively, which qualitatively agree with the results in Figs. 3(a) and (b). The accuracy of the phase diagram is limited by the finite evolution time, which is in turn set by the decoherence time. In our experiment, the decoherence is caused by imperfections in the system, such as off-resonant Bragg couplings, the inhomogeneity caused by the dipole trap, and inhomogeneous interactions between atoms [37, 41].

*Topological phase diagram:*— In Fig. 4(a), we show the time evolution of MCD under different parameters. The observed MCD oscillates around unity in region I with  $\delta/t = 0.5$ , whereas in region IV with  $\delta/t = 1.5$ , the MCD fluctuates around 0.5. A topological phase transition can therefore be identified through the A-MCD, as illustrated in Fig. 4(b), close to the theoretically predicted topological transition point  $\delta/t = 1.4$ . Similar to the case with dIPR, we map out the topological phase diagram using color contours in Fig. 4(c)(d). The experimentally measured A-MCD clearly indicates the presence of a topological phase transition at sufficiently large  $\delta$  [Fig. 4(c)], with the boundary of the transition consistent with both the numerical results [Fig. 4(d)] and the theoretical prediction [Fig. 1(b)]. Again, the accuracy of the measured phase diagram is limited by the experimentally achievable coherent evolution time (see Supplemental Information).

*Impact of interaction:*— Since inter-atomic interactions are tunable in cold atom gases, our system offers a perfect platform to study interaction effects, which, in a disordered system, can lead to intriguing states of matter such as many-body localized or many-body critical phases. The inter-atomic collisions in our system can be effectively modeled, on the mean-field level, as attractive on-site interactions governed by the Hamiltonian [34, 36]

$$\hat{H}_{\text{int}} = U \sum_j (2 - \langle \hat{n}_j \rangle) \hat{n}_j. \quad (6)$$

Here, the number operator  $\hat{n}_j = \hat{c}_j^\dagger \hat{c}_j$ , and  $\langle \hat{n}_j \rangle$  is the normalized atomic population on site  $j$ . While we vary the ratio between the interaction and kinetic energies  $U/t$  by adjusting the total number of atoms in the BEC, we now fix a smaller hopping rate  $t \approx 2\pi \times 0.5\text{kHz}$  and larger trapping frequencies  $2\pi \times (70, 240, 250)\text{Hz}$ , so that  $U/t$  is tunable over a wider range up to  $U/t \sim 3.2$ .

Figures 5(a)(b) contrast experimentally measured localization phase diagrams with different values of  $U/t$ . With a larger  $U/t$ , the stability region of the extended

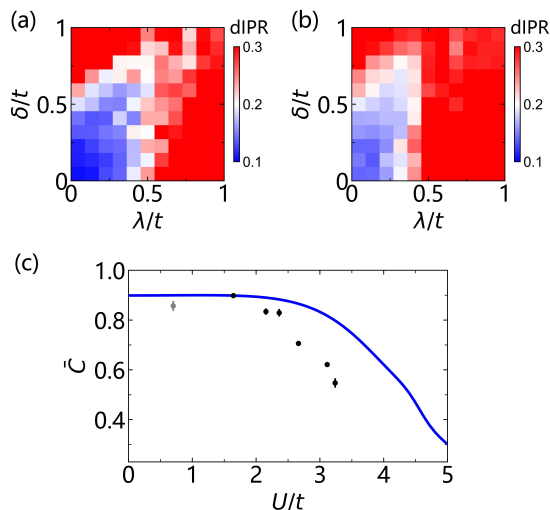


FIG. 5. Impact of interaction. (a)(b) Experimentally measured dIPR under different interaction energy  $U$ , with (a)  $U/\hbar \approx 2\pi \times 0.8(2)$  kHz and (b)  $U/\hbar \approx 2\pi \times 1.7(4)$  kHz. (c) A-MCD as a function of  $U/t$  for  $\lambda/t = 0.2$  and  $\delta/t = 0.2$ . Black dots are experimental data and the blue line is the numerical result under the same parameters. Both experimental and numerical results are performed on a lattice of 16 sites, with  $t/\hbar = 2\pi \times 0.50(5)$  kHz and a total evolution time of 1ms. The gray dot in (c) represents the corresponding experimental data in Fig. 4. Error bars show SE of mean.

state becomes smaller, while the region of critical localization increases. This is consistent with previous studies of interaction effects in momentum lattices, where interactions facilitate localization [37] (see the Supplemental Information). On the other hand, in the topologically non-trivial regime, shown in Fig. 5(c), the measured A-MCD remains quantized upto  $U/t \sim 2$ , indicating the robustness of the topological phase against small interactions. Under stronger interactions, however, the A-MCD appreciably deviates from unity, suggesting an interaction-induced topological phase transition.

*Discussion and outlook:*— We report the experimental observation of a critically localized topological state which is robust under small interactions. Exploiting the flexible control available to cold atoms in a momentum lattice, we show that interactions can enlarge the stability region of the critical phase. In future studies, it would be desirable to incorporate Feshbach resonance [42–44] to enlarge the tuning range of interactions, which would be valuable for the study of many-body critical and many-body localized phases. It would also be interesting to introduce on-site disorder on top of our model, under which a critical to fully-localized phase transition should occur [27]. Our experiment is a first step toward the preparation and probe of many-body critical states, and establishes a versatile platform on which the interplay of localization, topology and interaction can be investigated systematically. Our results would also stimulate further

study on the interaction-induced topological phase transitions in a disordered system.

*Acknowledgement:*— B. Y. acknowledge the support from the National Key Research and Development Program of China under Grant No. 2018YFA0307200, the National Natural Science Foundation of China under Grant No. 12074337, Natural Science Foundation of Zhejiang province under Grant No. LZ18A040001, Zhejiang Province Plan for Science and technology No. 2020C01019 and the Fundamental Research Funds for the Central Universities. W. Y. acknowledges support from the National Natural Science Foundation of China under Grant Nos. 11974331, the National Key Research and Development Program of China under Grant Nos. 2016YFA0301700 and 2017YFA0304100.

\* These authors contributed equally to this work

† wyiz@ustc.edu.cn

‡ yanbohang@zju.edu.cn

- [1] M. Z. Hasan and C. L. Kane, Rev. Mod. Phys. **82**, 3045 (2010).
- [2] X.-L. Qi and S.-C. Zhang, Rev. Mod. Phys. **83**, 1057 (2011).
- [3] P. W. Anderson, Phys. Rev. **109**, 1492 (1958).
- [4] J. Billy, V. Josse, Z. Zuo, A. Bernard, B. Hambrecht, P. Lugan, D. Clement, L. Sanchez-Palencia, P. Bouyer, and A. Aspect, Nature **453**, 891 (2008).
- [5] G. Roati, C. D’Errico, L. Fallani, M. Fattori, C. Fort, M. Zaccanti, G. Modugno, M. Modugno, and M. Inguscio, Nature **453**, 895 (2008).
- [6] S. S. Kondov, W. R. McGehee, J. J. Zirbel, and B. DeMarco, Science **334**, 66 (2011).
- [7] J. Li, R.-L. Chu, J. K. Jain, and S.-Q. Shen, Phys. Rev. Lett. **102**, 136806 (2009).
- [8] H.-M. Guo, G. Rosenberg, G. Refael, and M. Franz, Phys. Rev. Lett. **105**, 216601 (2010).
- [9] H. Jiang, L. Wang, Q.-f. Sun, and X. C. Xie, Phys. Rev. B **80**, 165316 (2009).
- [10] A. Altland, D. Bagrets, L. Fritz, A. Kamenev, and H. Schmiedt, Phys Rev Lett **112**, 206602 (2014).
- [11] I. Mondragon-Shem, T. L. Hughes, J. Song, and E. Prodan, Phys. Rev. Lett. **113**, 046802 (2014).
- [12] C. Liu, W. Gao, B. Yang, and S. Zhang, Phys. Rev. Lett. **119**, 183901 (2017).
- [13] A. Agarwala and V. B. Shenoy, Phys. Rev. Lett. **118**, 236402 (2017).
- [14] R. Chen, D.-H. Xu, and B. Zhou, Phys. Rev. B **100**, 115311 (2019).
- [15] L.-Z. Tang, L.-F. Zhang, G.-Q. Zhang, and D.-W. Zhang, Phys. Rev. A **101**, 063612 (2020).
- [16] E. J. Meier, F. A. An, A. Dauphin, M. Maffei, P. Massignan, T. L. Hughes, and B. Gadway, Science **362**, 929 (2018).
- [17] S. Stutzer, Y. Plotnik, Y. Lumer, P. Titum, N. H. Lindner, M. Segev, M. C. Rechtsman, and A. Szameit, Nature **560**, 461 (2018).
- [18] G.-G. Liu, Y. Yang, X. Ren, H. Xue, X. Lin, Y.-H. Hu, H.-X. Sun, B. Peng, P. Zhou, Y. Chong, and B. Zhang,

- Phys. Rev. Lett. **125**, 133603 (2020).
- [19] T. Geisel, R. Ketzmerick, and G. Petschel, Phys. Rev. Lett. **66**, 1651 (1991).
  - [20] K. Machida and M. Fujita, Phys. Rev. B **34**, 7367 (1986).
  - [21] A. D. Mirlin, Y. V. Fyodorov, A. Mildenerger, and F. Evers, Phys. Rev. Lett. **97**, 046803 (2006).
  - [22] Y. Takada, K. Ino, and M. Yamanaka, Phys. Rev. E **70**, 066203 (2004).
  - [23] J. Wang, X.-J. Liu, G. Xianlong, and H. Hu, Phys. Rev. B **93**, 104504 (2016).
  - [24] C. L. Bertrand and A. M. García-García, Phys. Rev. B **94**, 144201 (2016).
  - [25] J. C. C. Cestari, A. Foerster, and M. A. Gusmão, Phys. Rev. B **93**, 205441 (2016).
  - [26] T. Liu, P. Wang, and X. Gao, arXiv:1609.06939 (2016).
  - [27] Y. Wang, X.-j. Liu, and D. Yu, arXiv:1910.12080 (2019).
  - [28] Y. Wang, L. Zhang, S. Niu, D. Yu, and X.-J. Liu, Phys. Rev. Lett. **125**, 073204 (2020).
  - [29] M. Schreiber, S. S. Hodgman, P. Bordia, H. P. Lüschen, M. H. Fischer, R. Vosk, E. Altman, U. Schneider, and I. Bloch, Science **349**, 842 (2015).
  - [30] H. P. Luschen, S. Scherg, T. Kohlert, M. Schreiber, P. Bordia, X. Li, S. Das Sarma, and I. Bloch, Phys. Rev. Lett. **120**, 160404 (2018).
  - [31] M. Rispoli, A. Lukin, R. Schittko, S. Kim, M. E. Tai, J. Léonard, and M. Greiner, Nature **573**, 385 (2019).
  - [32] D. A. Abanin, E. Altman, I. Bloch, and M. Serbyn, Rev. Mod. Phys. **91**, 021001 (2019).
  - [33] E. J. Meier, F. A. An, and B. Gadway, Phys. Rev. A **93**, 051602 (2016).
  - [34] F. A. An, E. J. Meier, J. Ang'ong'a, and B. Gadway, Phys. Rev. Lett. **120**, 040407 (2018).
  - [35] F. A. An, E. J. Meier, and B. Gadway, Phys. Rev. X **8**, 031045 (2018).
  - [36] D. Xie, W. Gou, T. Xiao, B. Gadway, and B. Yan, npj Quan. Inf. **5**, 55 (2019).
  - [37] D. Xie, T.-S. Deng, T. Xiao, W. Gou, T. Chen, W. Yi, and B. Yan, Phys. Rev. Lett. **124**, 050502 (2020).
  - [38] F. Cardano, A. D'Errico, A. Dauphin, M. Maffei, B. Piccirillo, C. de Lisio, G. De Filippis, V. Cataudella, E. Santamato, L. Marrucci, M. Lewenstein, and P. Massignan, Nat. Comm. **8**, 15516 (2017).
  - [39] W. P. Su, J. R. Schrieffer, and A. J. Heeger, Phys. Rev. Lett. **42**, 1698 (1979).
  - [40] E. J. Meier, F. A. An, and B. Gadway, Nat. Comm. **7**, 13986 (2016).
  - [41] W. Gou, T. Chen, D. Xie, T. Xiao, T.-S. Deng, B. Gadway, W. Yi, and B. Yan, Phys. Rev. Lett. **124**, 070402 (2020).
  - [42] A. Marte, T. Volz, J. Schuster, S. Dürr, G. Rempe, E. G. M. van Kempen, and B. J. Verhaar, Phys. Rev. Lett. **89**, 283202 (2002).
  - [43] N. Syassen, T. Volz, S. Teichmann, S. Dürr, and G. Rempe, Phys. Rev. A **74**, 062706 (2006).
  - [44] G. Thalhammer, M. Theis, K. Winkler, R. Grimm, and J. H. Denschlag, Phys. Rev. A **71**, 033403 (2005).
  - [45] S. Longhi, arXiv:2008.06493 (2020).
  - [46] I. C. Fulga, F. Hassler, A. R. Akhmerov, and C. W. J. Beenakker, Phys. Rev. B **83**, 155429 (2011).

## Supplemental Information for “Observation of topological phase with critical localization in a quasi-periodic lattice”

In the Supplemental Information, we provide details for the experimental setup, features of edge states, theoretical analysis of topological number and localization length, details on the calculation of mean chiral displacement, and interaction effects.

### Experimental implementation of the off-diagonal Aubry-André model

Following the practice in Refs. [16, 36, 41], we generate a one-dimensional momentum lattice for a Bose-Einstein condensate (BEC) of  $^{87}\text{Rb}$  atoms loaded in a crossed dipole trap. The trapping frequencies are chosen such that the atoms are only weakly trapped along the direction of the momentum lattice, but are strongly trapped in other directions. As illustrated in Fig. S1(a), discrete momentum states are resonantly coupled, along the weakly-trapped direction, by pairs of counter-propagating 1064nm Bragg lasers. By engineering the frequencies of the multi-component Bragg lasers, a one-dimensional momentum lattice with adjacent sites separated by  $2\hbar k$  is created, whose nearest-neighbor hopping rates can be tailored by individually tuning the coupling strengths of the Bragg processes. Here  $k$  is the wave number of the 1064nm laser. For the quasi-periodic disorder in particular, we modulate the amplitude of the Bragg beam with frequency  $\omega_j$  with the function  $[1 + \lambda/t \cos(j+1)\pi + \delta/t \cos(2\pi\beta j + \varphi)]$  (see main text for definition of variables), while the frequency  $\omega_j$  is tuned to the two-photon resonance between the corresponding momentum states [see Fig. S1(b)], via an acousto-optic modulator.

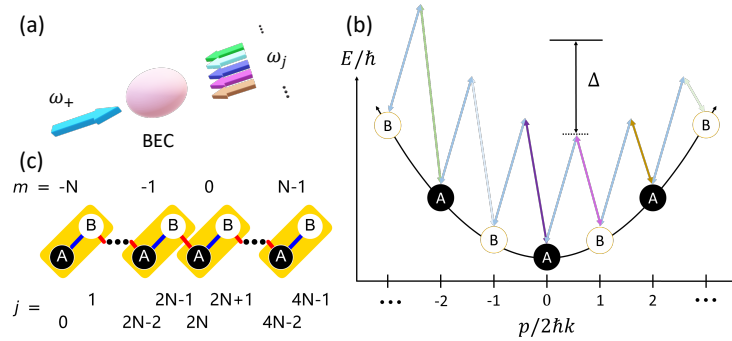


FIG. S1. Generating the one-dimensional momentum lattice. (a) Bragg-coupling scheme. (b) Pairs of counter-propagating Bragg lasers with fine-detuned frequencies ( $\omega_+$  and  $\omega_j$ ) couple adjacent momentum lattice sites. (c) A schematic illustration of the resulting one-dimensional momentum lattice.

### Zero-energy and isolated edged states

In Fig. S2(a), we show the complete eigenenergy spectrum under an open boundary condition, with  $\lambda/t = 0.4$ . Both the zero-energy and isolated edge states are shown in red, with their density distributions plotted in Fig. S2(c) (zero-energy), and Figs. S2(d) (isolated), respectively. The zero-energy edge states are topological, with their appearance/disappearance consistent the topological phase diagram shown in Fig. 1(b) of the main text. From the  $\text{IPR}_n$  calculation in Fig. S2(b) [as well as in Fig. 1(c) of the main text], our model does not possess mobility edges, since the extended to critical localization transition occurs at the same point for all eigenstates (excluding the edge states). Further, beyond the extended to critical transition at  $\delta/t = 0.6$ , the calculated  $\text{IPR}_n$  for all eigenstates become finite [see Fig. S2(b)], but still appreciably smaller than unity, confirming their critically localized nature.

### Mean chiral displacement

For our measurements of time-averaged mean chiral displacement (A-MCD) in the main text, the atoms are initialized on the site  $|m = 0, A\rangle$ . More generally, A-MCD is sensitive to the initially populated sublattice site. To see

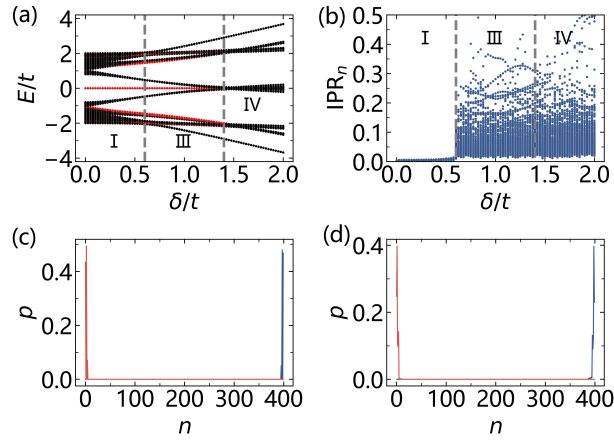


FIG. S2. Eigenenergy spectrum and edge states. (a) Eigenenergy spectrum for  $\lambda/t = 0.4$ , with edge states (both zero-energy edge states and other isolated edge states) marked in red. (b)  $\text{IPR}_n$  for all bulk eigenstates (edge states excluded) with increasing disorder strength  $\delta/t$  for  $\lambda/t = 0.4$ . (c) Density distribution  $p$  of zero-energy edge states with  $\lambda/t = 0.4$  and  $\delta/t = 0.5$ . (d) Density distribution  $p$  of a typical pair of isolated edge states with  $\lambda/t = 0.4$  and  $\delta/t = 0.5$ . For all panels, we take  $\varphi = 0$ .

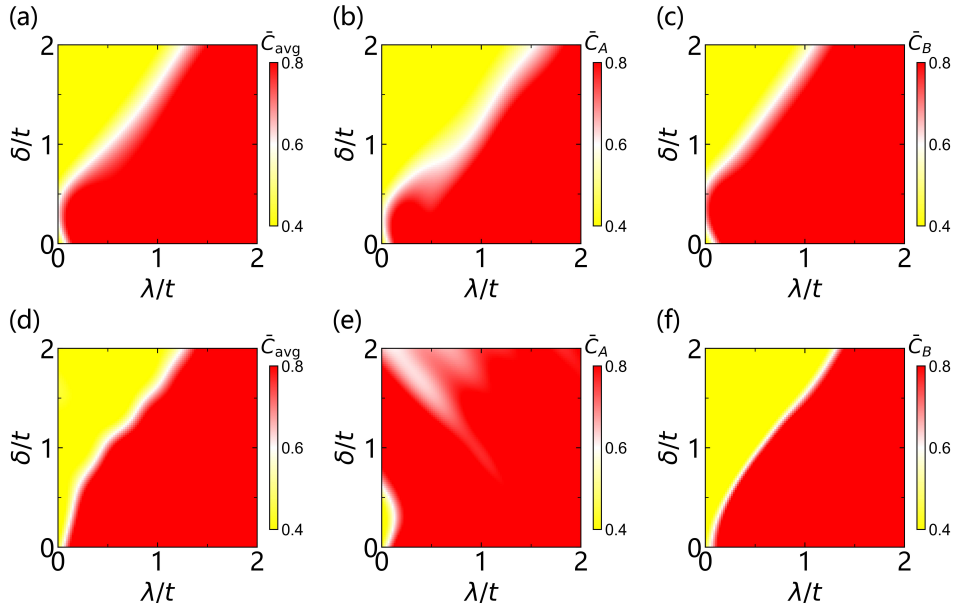


FIG. S3. Numerical simulation of different definitions of A-MCDs,  $\bar{C}_{\text{avg}}$ ,  $\bar{C}_A$ , and  $\bar{C}_B$ . (a)(b)(c) Comparison of A-MCDs on a lattice of 16 sites ( $N = 4$ ). (d)(e)(f) Comparison of A-MCDs on a lattice of 28 sites ( $N = 7$ ). For all calculations, we take an overall evolution time of 0.5ms with  $t/\hbar = 2\pi \times 1\text{kHz}$  and  $\varphi = 0$ , consistent with experimental parameters.

this point, we define

$$\bar{C}_\sigma(\tau) = 2\langle m = 0, \sigma | e^{i\hat{H}_0\tau} (\hat{\Gamma}\hat{m}) e^{-i\hat{H}_0\tau} | m = 0, \sigma \rangle, \quad (\text{S1})$$

where  $\sigma \in \{A, B\}$  indicates the initial sublattice site, and  $\tau$  stands for the evolution time. In Fig. S3, we show the numerically calculated A-MCDs  $\bar{C}_\sigma$ , as well as  $\bar{C}_{\text{avg}} = (\bar{C}_A + \bar{C}_B)/2$  on the  $\delta$ - $\lambda$  plane under different parameters. While under experimental parameters,  $\bar{C}_A$ ,  $\bar{C}_B$  and  $\bar{C}_{\text{avg}}$  are qualitatively the same and are consistent with the theoretical phase diagram [see Fig. S3(a)(b)(c)]; for other choices of parameters,  $\bar{C}_A$  and  $\bar{C}_B$  can be quite different [see Fig. S3(d)(e)(f)]. It is thus preferable to use  $\bar{C}_{\text{avg}}$  to characterize the A-MCD in general. Alternatively, we find that, by averaging over randomly chosen  $\varphi$ ,  $\bar{C}_A$  and  $\bar{C}_B$  would converge to the same values [see Fig. 1(d)].

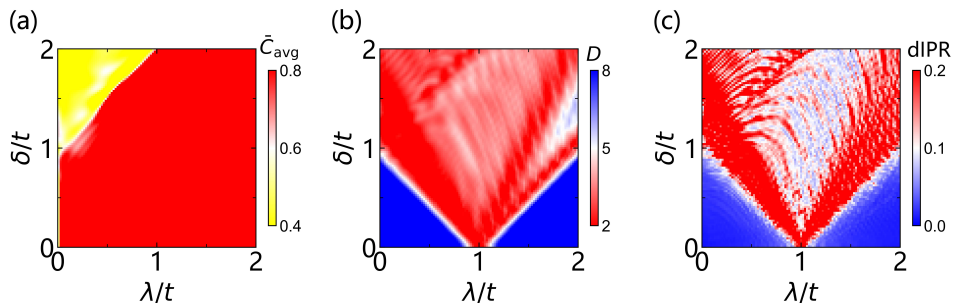


FIG. S4. Numerical simulation of (a)  $\bar{C}_{\text{avg}}$ , (b)  $D$ , and (c) dIPR for an evolution with the duration  $60\hbar/t$  on a lattice of 320 ( $N = 80$ ) sites. For the calculations, we fix the hopping rate as  $t/\hbar = 2\pi \times 1\text{kHz}$  and take  $\varphi = 0$ .

### Dynamic phase diagram from time evolutions with longer duration

A main factor that limits the accuracy of the dynamically determined phase diagrams is the finite evolution time achievable in our experiment, which is constrained by the decoherence time of the Bragg-coupled BEC. To explicitly demonstrate this, we numerically simulate a time evolution with a much longer duration, driven by the Hamiltonian (1), and plot the various dynamic quantities in Fig. S4. Apparently, given a sufficiently long evolution time, both the topological [Fig. S4(a)] and localization phase diagrams [Fig. S4(b)(c)] are well-captured by dynamic quantities such as A-MCD, mean displacement  $D$ , and dIPR, as all phase diagrams are consistent with the theoretically predicted one in Fig. 1(b) of the main text.

### Topological number and localization length of the off-diagonal Aubry-André model

While both the local topological marker (LTM) and A-MCD are able to characterize the topological phase boundary, in the critically localized, topologically trivial region (region IV), LTM and A-MCD seem to spread around a half-integer value of 0.5 rather than around zero. Such a phenomenon is related to the apparent divergence of the localization length as well as the closing of the band gap in the entire region IV.

According to Refs. [45, 46], the topological number  $\nu$  of our model can be written as

$$\nu = \frac{1}{2}(1 - \nu'), \quad (\text{S2})$$

where

$$\begin{aligned} \nu' &= \text{sign} \left\{ \prod_j [1 - \lambda + \delta \cos(2\pi\beta \times 2j)]^2 - \prod_j [1 + \lambda + \delta \cos(2\pi\beta \times (2j + 1))]^2 \right\} \\ &= \text{sign} \left( \prod_j S_1^{2N} - \prod_j S_2^{2N} \right), \end{aligned} \quad (\text{S3})$$

with

$$\log S_1 = \lim_{N \rightarrow \infty} \frac{1}{N} \sum_{j=0}^N \log |1 - \lambda + \delta \cos(2\pi\beta \times 2j)|, \quad (\text{S4})$$

$$\log S_2 = \lim_{N \rightarrow \infty} \frac{1}{N} \sum_{j=0}^N \log |1 + \lambda + \delta \cos[2\pi\beta \times (2j + 1)]|. \quad (\text{S5})$$

Here we set the nearest-neighbor hopping rate  $t$  as the unit of energy. For the convenience of discussion, we define

$$W = \log S_2 - \log S_1. \quad (\text{S6})$$

Applying the Weyl's equidistribution theorem and converting the summations above to integrals, we have the following results

$$W = \begin{cases} > 0, & \text{for } \delta \leq 1 + \lambda \\ 0, & \text{for } \delta > 1 + \lambda \end{cases}, \quad (\text{S7})$$

which leads to

$$\nu = \begin{cases} 1, & \text{for } \delta \leq 1 + \lambda \\ 0.5, & \text{for } \delta > 1 + \lambda \end{cases}. \quad (\text{S8})$$

This is consistent with numerical results in Fig. 1(d) of the main text, where both LTM and A-MCD appear to distribute around  $\nu = 0.5$  in region IV. However, while topological edge states disappear in region IV, the half-integer value of  $\nu$  therein does not correspond to the number of edge states under an open boundary condition. We attribute such a reality to the closing of the bulk gap in region IV, which invalidates  $\nu$  as a topological invariant.

The analysis above can also be understood in terms of the inverse localization length  $\Lambda^{-1}$  calculated from the transfer matrix. More specifically, we consider the Schrödinger's equation for the zero-energy state  $|\Psi\rangle = \sum_j \Psi(j)c_j^\dagger|\text{vac}\rangle$

$$\hat{H}_0|\Psi\rangle = 0, \quad (\text{S9})$$

which leads to

$$\Psi(N) = (-1)^N \prod_{j=0}^{N-1} \frac{1 + \lambda + \delta \cos[2\pi\beta \times (2j + 1)]}{1 - \lambda + \delta \cos(2\pi\beta \times 2j)} \Psi(1). \quad (\text{S10})$$

It follows that [11]

$$\Lambda^{-1} = \lim_{N \rightarrow \infty} \frac{1}{N} \log \left| \frac{\Psi(N)}{\Psi(1)} \right| \quad (\text{S11})$$

$$= \left| \lim_{N \rightarrow \infty} \frac{1}{N} \sum_{j=0}^{N-1} (\log |1 + \lambda + \delta \cos[2\pi\beta \times (2j + 1)]| - \log |1 - \lambda + \delta \cos(2\pi\beta \times 2j)|) \right| \quad (\text{S12})$$

$$= |\log S_2 - \log S_1| \quad (\text{S13})$$

$$= |W|. \quad (\text{S14})$$

Therefore,  $\Lambda^{-1} = 0$  for  $\delta > 1 + \lambda$ , i.e., the localization length diverges in the entire region IV. Physically, such a result derives from the fact that the quasi-periodic disorder is imposed on both the inter- and intra-cell couplings. If, for instance, one adopts a model where quasi-periodic disorder is only imposed on the inter- or intra-cell hopping rates, the band gap would open up in the topologically trivial region, with a vanishing topological invariant  $\nu$ . The localization length then would only diverge on the boundary of the topological phase transition.

### Interaction effect

To supplement Fig. 5 of the main text in depicting the interaction effects, we numerically simulate dynamics under the mean-field Hamiltonian  $\hat{H}_0 + \hat{H}_{\text{int}}$  for a longer evolution time of  $60\hbar/t$ , with either small [Fig. S5(a)(b)] or large [Fig. S5(c)(d)] interaction energy. The resulting topological and localization phase diagrams in terms of  $\bar{C}_{\text{avg}}$  and dIPR are shown in Fig. S5(a)(c) and (b)(d), respectively. Compared with the non-interacting case in Fig. S4, phase diagrams in Fig. S5(a)(b) are almost the same, indicating the robustness of phase boundaries under small interactions. However, both the topological and localization phase boundaries are shifted under larger interactions, leading to a larger stability region of the critically localized topological phase in Fig. S5(c)(d). The long-time numerical simulation thus supports our conclusions in the main text.

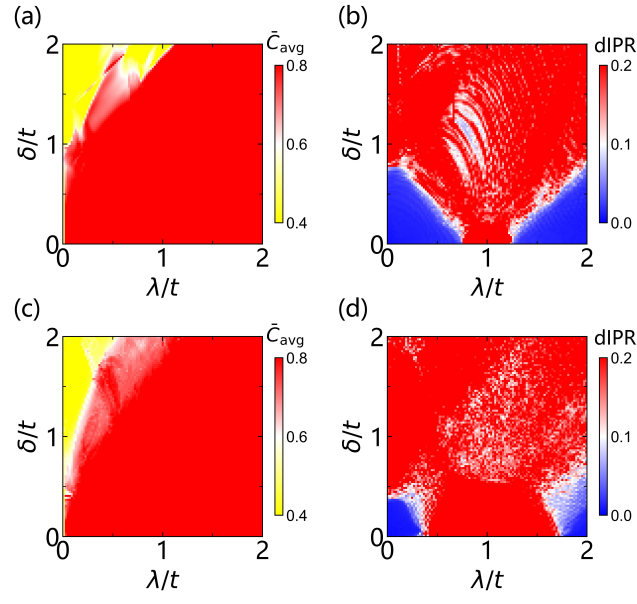


FIG. S5. Numerical simulation of (a)(c)  $\bar{C}_{\text{avg}}$  and (b)(d) dIPR. The interaction parameter is  $U/t = 0.7$  in (a)(b), and  $U/t = 2$  in (c)(d). Other parameters are same as those in Fig. S4.